



## OPEN ACCESS

## EDITED BY

Junjie Li,  
Innovation Centre of NanoMedicine  
(iCONM), Japan

## REVIEWED BY

Xiaoyuan Li,  
Northeast Normal University, China  
Qinghao Zhou,  
University of Science and Technology of  
China, China

## \*CORRESPONDENCE

Murugan Ramalingam,  
rmurug2000@gmail.com  
ShuYang Xie,  
shuyangxie@aliyun.com  
RanRan Wang,  
wangrr@bzmc.edu.cn

<sup>†</sup>These authors have contributed equally  
to this work

## SPECIALTY SECTION

This article was submitted  
to Biomaterials,  
a section of the journal  
Frontiers in Bioengineering and  
Biotechnology

RECEIVED 28 July 2022

ACCEPTED 19 August 2022

PUBLISHED 13 September 2022

## CITATION

Li X, Gao Y, Liu X, Hu X, Li Y, Sun J,  
Wang P, Wu H, Kim H, Ramalingam M,  
Xie S and Wang R (2022), Ultrasound and  
laser-promoted dual-gas nano-  
generator for combined photothermal  
and immune tumor therapy.  
*Front. Bioeng. Biotechnol.* 10:1005520.  
doi: 10.3389/fbioe.2022.1005520

## COPYRIGHT

© 2022 Li, Gao, Liu, Hu, Li, Sun, Wang,  
Wu, Kim, Ramalingam, Xie and Wang.  
This is an open-access article  
distributed under the terms of the  
[Creative Commons Attribution License  
\(CC BY\)](https://creativecommons.org/licenses/by/4.0/). The use, distribution or  
reproduction in other forums is  
permitted, provided the original  
author(s) and the copyright owner(s) are  
credited and that the original  
publication in this journal is cited, in  
accordance with accepted academic  
practice. No use, distribution or  
reproduction is permitted which does  
not comply with these terms.

# Ultrasound and laser-promoted dual-gas nano-generator for combined photothermal and immune tumor therapy

XinYu Li<sup>1,2†</sup>, Yong Gao<sup>3†</sup>, XinZheng Liu<sup>1,2</sup>, XiaoQian Hu<sup>1</sup>,  
YunMeng Li<sup>1</sup>, JunXi Sun<sup>1</sup>, PingYu Wang<sup>4</sup>, Hongkai Wu<sup>5</sup>,  
HaeWon Kim<sup>6,7,8</sup>, Murugan Ramalingam<sup>6,7,8,9\*</sup>, ShuYang Xie<sup>4\*</sup>  
and RanRan Wang<sup>1,2\*</sup>

<sup>1</sup>Institute of Rehabilitation Medicine, School of Rehabilitation Medicine, Binzhou Medical University, Yantai, China, <sup>2</sup>Shandong Laboratory of Advanced Materials and Green Manufacturing, Yantai, China, <sup>3</sup>Binzhou Medical University Hospital, Binzhou, China, <sup>4</sup>Key Laboratory of Tumor Molecular Biology, Binzhou Medical University, Yantai, China, <sup>5</sup>Department of Chemistry, The Hong Kong University of Science and Technology, Hong Kong, China, <sup>6</sup>Institute of Tissue Regeneration Engineering, Dankook University, Cheonan, Korea, <sup>7</sup>Department of Nanobiomedical Science, BK21 NBM Global Research Center for Regenerative Medicine, Dankook University, Cheonan, Korea, <sup>8</sup>Mechanobiology Dental Medicine Research Center, Dankook University, Cheonan, Korea, <sup>9</sup>School of Basic Medical Sciences, Chengdu University, Chengdu, China

The combination of photothermal therapy (PTT) and immune tumor therapy has emerged as a promising avenue for cancer treatment. However, the insufficient immune response caused by inefficient immunogenic cell death (ICD) inducers and thermal resistance, immunosuppression, and immune escape resulting from the hypoxic microenvironment of solid tumors severely limit its efficacy. Herein, we report an ultrasound and laser-promoted dual-gas nano-generator (calcium carbonate-polydopamine-manganese oxide nanoparticles, CPM NPs) for enhanced photothermal/immune tumor therapy through reprogramming tumor hypoxic microenvironment. In this system, CPM NPs undergo reactive decomposition in a moderately acidic tumor, resulting in the generation of calcium, manganese ions, carbon dioxide (CO<sub>2</sub>), and oxygen (O<sub>2</sub>). Calcium and manganese ions act as adjuvants that trigger an immune response. The cancer cell membrane rupture caused by sudden burst of bubbles (CO<sub>2</sub> and O<sub>2</sub>) under ultrasound stimulation and the photothermal properties of PDA also contributed to the ICD effect. The generation of O<sub>2</sub> alleviates tumor hypoxia and thus reduces hypoxia-induced heat resistance and immunosuppressive effects, thereby improving the therapeutic efficacy of combination PTT and immune therapy. The present study provides a novel approach for the fabrication of a safe and effective tumor treatment platform for future clinical applications.

## KEYWORDS

CaCO<sub>3</sub>-PDA-MnO<sub>2</sub> nanoparticles, dual-gas nano-generator, ultrasound and laser, photothermal, immunotherapy

## Introduction

Cancer is the second most common cause of death, seriously threatening human health (Liu J et al., 2019; Soerjomataram and Bray, 2021). Various treatment modalities such as surgery, radiotherapy, and chemotherapy have been used to eliminate tumors. However, the disadvantages of severe trauma, poor selectivity, and drug resistance greatly limit the application of these methods. Photothermal therapy (PTT) as an effective tumor treatment modality with non-invasive, highly targeted, low systemic toxicity and few side effects has got widespread attentions. PTT kills tumor cells by converting light energy into heat energy, and has received extensive attention (Li et al., 2018). However, in addition to effective tumor growth inhibition, avoiding tumor recurrence is crucial for effective tumor treatment. Immunotherapy, a rapidly developing therapeutic approach that inhibits tumor growth and prevents tumor recurrence and metastasis by activating the immune system, is considered to be one of the most promising therapeutic techniques for tumors. Since immunogenic cell death (ICD) plays a significant role in initiating antitumor immune responses, the development of potent ICD inducers is required to improve the efficacy of immunotherapy (Duan et al., 2019; Liu P et al., 2019; Chattopadhyay et al., 2020; Ding et al., 2020). Various ICD inducers have been reported, including radiation (Chao et al., 2018), photosensitizers (Deng et al., 2020), and chemotherapeutic drugs (Nam et al., 2018). However, X-rays and drug molecules can cause systemic toxicity and drug resistance, thereby increasing the risk of treatment. Therefore, development of mild and non-drug ICD inducers is required for safe and efficient immunotherapy. Currently, in addition to selecting efficient ICD inducers, remodeling the tumor hypoxic microenvironment is another important strategy to improve the immunotherapy efficiency (Hu et al., 2020; Li and Kataoka, 2021). Recently,  $\text{Ca}^{2+}$  has been reported to serve as an ICD inducer in immunotherapy. ICD effects are attributed to mitochondrial  $\text{Ca}^{2+}$  overload and the subsequent upregulation of the reactive oxygen species (ROS) levels (Zheng et al., 2021). Furthermore, exogenous ultrasound (US) stimuli can enhance  $\text{Ca}^{2+}$  overload by promoting  $\text{Ca}^{2+}$  influx from the extracellular fluid to the cytoplasm, resulting in enhanced ICD (Samal et al., 2000; Parvizi et al., 2002; Park et al., 2010). Another report showed that the sudden burst  $\text{CO}_2$  bubbles in the tumor microenvironment can also stimulate efficient immunogenicity by inducing membrane rupture of cancer cells (Jeon et al., 2022). Several studies have demonstrated that PTT can not only directly destroy tumor cells but also indirectly stimulate systemic immunity (Jiao et al., 2021; Yasothamani et al., 2021); therefore, the combined treatment using PTT and an ICD-inducer is anticipated to improve the efficiency of immunotherapy. Nevertheless, the hypoxic characteristics of tumors impair the efficiency of PTT and immunotherapy. For example, the hypoxic characteristics of tumor tissue leading to

thermal resistance, reducing the efficiency of photothermal treatment (Meng et al., 2018; Wen et al., 2020; Dai et al., 2021; Lv et al., 2021). Moreover, hypoxia can lead to immune suppression and escape (Riera-Domingo et al., 2020; Zhou et al., 2020).  $\text{MnO}_2$  nanoparticles with tumor microenvironment-responsive degradation characteristics and catalase properties can react with excess  $\text{H}_2\text{O}_2$  present in tumor tissue, producing  $\text{O}_2$  and  $\text{Mn}^{2+}$  to alleviate tumor hypoxia (Fan et al., 2015; Yang et al., 2017; Duan et al., 2020). In addition, recent studies have shown that  $\text{MnO}_2$  can be used as an immune adjuvant to trigger ICD by dual induction of  $\text{Mn}^{2+}$ -triggered chemodynamic therapy (CDT) and glutathione (GSH)-depleting ferroptosis (Lv et al., 2020). CDT and ferroptosis can stimulate dying cancer cells to produce damage-associated molecular patterns (DAMPs), thereby eliciting ICD (Chen Y et al., 2019; Wen et al., 2019; Zhang et al., 2019).

In this study, we constructed ultrasonication- and laser-promoted dual-gas nanogenerators based on calcium carbonate ( $\text{CaCO}_3$ ), polydopamine (PDA), and manganese oxide ( $\text{MnO}_2$ ) nanoparticles for combined photothermal/immune tumor therapy.  $\text{CaCO}_3$  has the characteristics of accessibility, good biocompatibility, and pH sensitivity and can decompose at the tumor site, generating carbon dioxide ( $\text{CO}_2$ ) and  $\text{Ca}^{2+}$  (Feng et al., 2018; Yu et al., 2018; Sun et al., 2019; Wang et al., 2020). The inherent photothermal properties of PDA make it suitable for PTT (Wang et al., 2018; Chen Q et al., 2019; Li et al., 2020).  $\text{MnO}_2$  can decompose into oxygen and manganese ions in the tumor microenvironment. Therapeutic systems do not involve chemical drugs, preventing drug resistance. When delivered to the tumor site, the CPM NPs undergo reactive decomposition in a moderately acidic tumor microenvironment, resulting in the generation of  $\text{Ca}^{2+}$ ,  $\text{Mn}^{2+}$ ,  $\text{CO}_2$ , and  $\text{O}_2$ . The generated  $\text{Ca}^{2+}$  and  $\text{Mn}^{2+}$  act as immune adjuvants to trigger ICD. The cancer cell membrane rupture caused by sudden burst of  $\text{CO}_2$ ,  $\text{O}_2$ , and the photothermal properties of PDA also contributed to ICD. The generation of  $\text{O}_2$  alleviates tumor hypoxia and thus reduces the hypoxia-induced heat resistance and immunosuppressive effects, thereby improving the therapeutic efficacy of PTT and immune therapy. In this treatment system, the combination of photothermal therapy and immunity can not only greatly inhibit tumor growth but also avoid tumor metastasis and secondary recurrence through immune effects. Finally, the tumor microenvironment-responsive degradation of the nanoparticles ensures their biosafety.

## Experimental details

### Materials

$\text{CaCl}_2$  and  $\text{NH}_4\text{HCO}_3$  were provided by Sinopharm Chemical Reagent Co., Ltd. (China). Dopamine was obtained

from Sigma-Aldrich. Manganese chloride ( $\text{MnCl}_2$ ) was provided by J and K Chemical Co. Singlet oxygen sensor green reagent was purchased from Meilunbio. Sodium hydroxide (NaOH) was provided by Tianjin Yongda Chemical Reagent Co., Ltd. Calcein-AM/propidium iodide (PI) was purchased from SolarBio. RPMI-1640 medium was purchased from Thermo Fisher Scientific, Inc. Fluorescein isothiocyanate (FITC) was provided by Biological Technology Co., Ltd. Lyso-Tracker Red and Fluo-4 AM were purchased from KeyGen Biotech Co., Ltd. 5,5',6,6'-Tetrachloro-1,1',3,3'-tetraethylbenzimidazolyl-carbocyanine chloride (JC-1) and mitochondrial extraction kit were purchased from Solarbio.

## Characterization

The morphology and size of the CPM NPs were analyzed using a JEM-1400 transmission electron microscope (TEM, JEOL, Japan). The size and surface charge of the  $\text{CaCO}_3$ -PDA (CP) and CPM NPs were analyzed using a Malvern Zetasizer Nano-ZS90 instrument (United Kingdom). X-ray photoelectron spectroscopy (XPS) spectra were obtained using a Thermo Fisher Scientific ESCALAB 250Xi XPS system. The concentration of  $\text{Ca}^{2+}$  in the CPM NPs was determined using inductively coupled plasma mass spectrometry (ICP-MS, Jena, PlasmaQuant<sup>®</sup> MS). Cell uptake was measured using a confocal laser-scanning microscope (CLSM ZEISS LSM 780, Carl Zeiss, Jena, Germany).

## Cell culture and animal studies

4T1 cells were cultured in RPMI-1640 medium containing 10% fetal bovine serum. Then, the cells were placed in an incubator containing 5%  $\text{CO}_2$  at 37°C. Healthy female BALB/c mice aged 5–7 weeks were provided by GemPharmatech Co., Ltd. (Nanjing, China). All animals were euthanized by dislocation of cervical vertebra after the treatments.

## Synthesis of calcium carbonate-polydopamine-manganese oxide nanoparticles

CP NPs were prepared *via* a one-pot gas diffusion method following previously reported procedures with some modifications (Dong et al., 2018). Briefly,  $\text{CaCl}_2$  (150 mg) mixed with dopamine (10 mg) was fully dissolved in anhydrous ethanol (100 ml). Then, the samples were transferred into a flask with  $\text{NH}_4\text{HCO}_3$  (5 g) and kept at 40°C for 24 h. Subsequently, CP NPs were obtained *via* centrifugation. To obtain CPM NPs, CP NPs (180 mg) were slowly dropped into an ethanol solution (30 ml) containing  $\text{MnCl}_2$  (360 mg). After stirring for 4 h, the Mn-ion-adsorbed CP nanoparticles were

collected by centrifugal purification. Then, NaOH (1 M) was mixed with the solution by adjusting the pH to 11 to obtain CPM NPs.

## Oxygen and reactive oxygen species generation *in vitro*.

The oxygen probe was immersed in different solutions (100  $\mu\text{M}$   $\text{H}_2\text{O}_2$ , pH 7.4 + CPM, pH 6.5 + CPM, pH 7.4 + CPM+100  $\mu\text{M}$   $\text{H}_2\text{O}_2$ , pH 6.5 + CPM+100  $\mu\text{M}$   $\text{H}_2\text{O}_2$ , and CPM 1 mg  $\text{ml}^{-1}$ ) to determine the oxygen concentration. ROS levels were assessed using an ROS probe (reagent singlet oxygen sensor green, SOSG). SOSG methanol solution (10  $\mu\text{L}$ , 2.5 M) was mixed into various solutions with CPM NPs (1 mg  $\text{ml}^{-1}$ ). Then, a 1,064 nm laser (1  $\text{W cm}^{-2}$ , 5 min) and/or US (1.0 MHz, 20% duty cycle, 0.5  $\text{W cm}^{-2}$ , 2 min) were applied to the mixture. Finally, a fluorescence spectrophotometer (Hitachi F-2700, Japan) was used to assess the SOSG signals of various groups.

## Investigation of $\text{Ca}^{2+}$ Release from calcium carbonate-polydopamine-manganese oxide nanoparticles *in vitro*.

CPM NPs (1 mg) were immersed in PBS (10 ml) at 37°C and different pH (7.4, 6.5, and 5.5). Supernatants were collected from each sample at 0, 4, 8, 12, and 16 h. The amount of released  $\text{Ca}^{2+}$  was measured by Inductively coupled plasma mass spectrometry (ICP-MS). The release fractions of  $\text{Ca}^{2+}$  were calculated as the amount of released  $\text{Ca}^{2+}$  from CPM NPs divided by the total amount of  $\text{Ca}^{2+}$  in CPM NPs.

## Antitumor therapy *in vitro*

The antitumor effect and biocompatibility of the CPM NPs were determined using the MTT assay. 4T1 cells were co-cultured with CPM NPs at various concentrations for 12 h. The antitumor effect of CPM NPs was measured after the treatment with a 1,064 nm laser (1  $\text{W cm}^{-2}$ , 5 min) and/or US (1.0 MHz, 20% duty cycle, 0.5  $\text{W cm}^{-2}$ , 2 min). Thereafter, the cell survival rate was measured after adding a medium containing MTT and incubating for 4 h. For live/dead staining, CPM NPs were co-incubated with 4T1 cells for 12 h. Subsequently, the Calcein-AM/PI probe was added to the cell medium after the treatment with the laser and/or ultrasonication and was incubated for 30 min. Finally, images were obtained by CLSM. For apoptosis, CPM NPs (20  $\mu\text{g ml}^{-1}$ ) were added to the 4T1 cells and cultured for 12 h. Thereafter, various treatments were applied to the cells. After 2 h, the cells were stained with annexin V-FITC/PI for flow cytometry detection.

## Detection of intracellular reactive oxygen species levels

Various conditions were detected using dichloro-dihydro-fluorescein diacetate (DCFH-DA) reagent (PBS, CPM, CPM + US, CPM + L, CPM + US + L, CPM: 20  $\mu\text{g ml}^{-1}$ , 1,064 nm laser: 1  $\text{W cm}^{-2}$ , 5 min and US: 1.0 MHz, 20% duty cycle, 0.5  $\text{W cm}^{-2}$ , 2 min) to generate intracellular ROS. The 4T1 cells plated on confocal dishes were co-incubated with CPM NPs for 12 h in the dark. Thereafter, the cells were treated by various treatments. Finally, CLSM was used to examine the fluorescence images.

## Lysosome escape

CPM NPs (labeled with FITC; 20  $\mu\text{g ml}^{-1}$ ) were added to 4T1 cells and incubated for 0.5, 1, and 4 h. Then, the cells were labeled with Lyso-Tracker Red (1  $\mu\text{M}$ ). After 4 h, a 1,064 nm laser (1  $\text{W cm}^{-2}$ , 5 min) and/or US (1.0 MHz, 20% duty cycle, 0.5  $\text{W cm}^{-2}$ , 2 min) were applied to the cells, and 4% paraformaldehyde solution was added to fix the cells. After 10 min of fixation, DAPI was added to stain the cells. Fluorescence images were obtained by CLSM after 10 min.

## JC-1 Staining to Measure Mitochondrial Membrane Potential

CPM NPs (20  $\mu\text{g ml}^{-1}$ ) were incubated with the 4T1 cells for 12 h. After various treatments, JC-1 (10  $\mu\text{g ml}^{-1}$ ) was incubated with cells within 10 min. Subsequently, the mitochondrial membrane potentials were visualized using CLSM images.

## Mitochondrial swelling study

The 4T1 cells were incubated with CPM NPs (20  $\mu\text{g ml}^{-1}$ ) for 12 h. After various treatments, the mitochondria of the 4T1 cells in various groups were extracted using a mitochondrial extraction kit, and mitochondrial swelling was analyzed by UV-Vis-NIR spectrophotometry to determine the optical intensity of the mitochondria at 540 nm.

## Intracellular $\text{Ca}^{2+}$ detection in 4T1 cells

CPM NPs (20  $\mu\text{g ml}^{-1}$ ) were cultured with 4T1 cells for 0, 1, and 4 h. Subsequently, Fluo-4 AM (1  $\mu\text{M}$ ) was used to label cells after incubation for 4 h. Then, a 1,064 nm laser (1  $\text{W cm}^{-2}$ , 5 min) and/or US (1.0 MHz, 20% duty cycle, 0.5  $\text{W cm}^{-2}$ , 2 min) were applied to the cells. Finally, fluorescence images were visualized by CLSM after co-incubation with Hoechst 33,342 for 10 min.

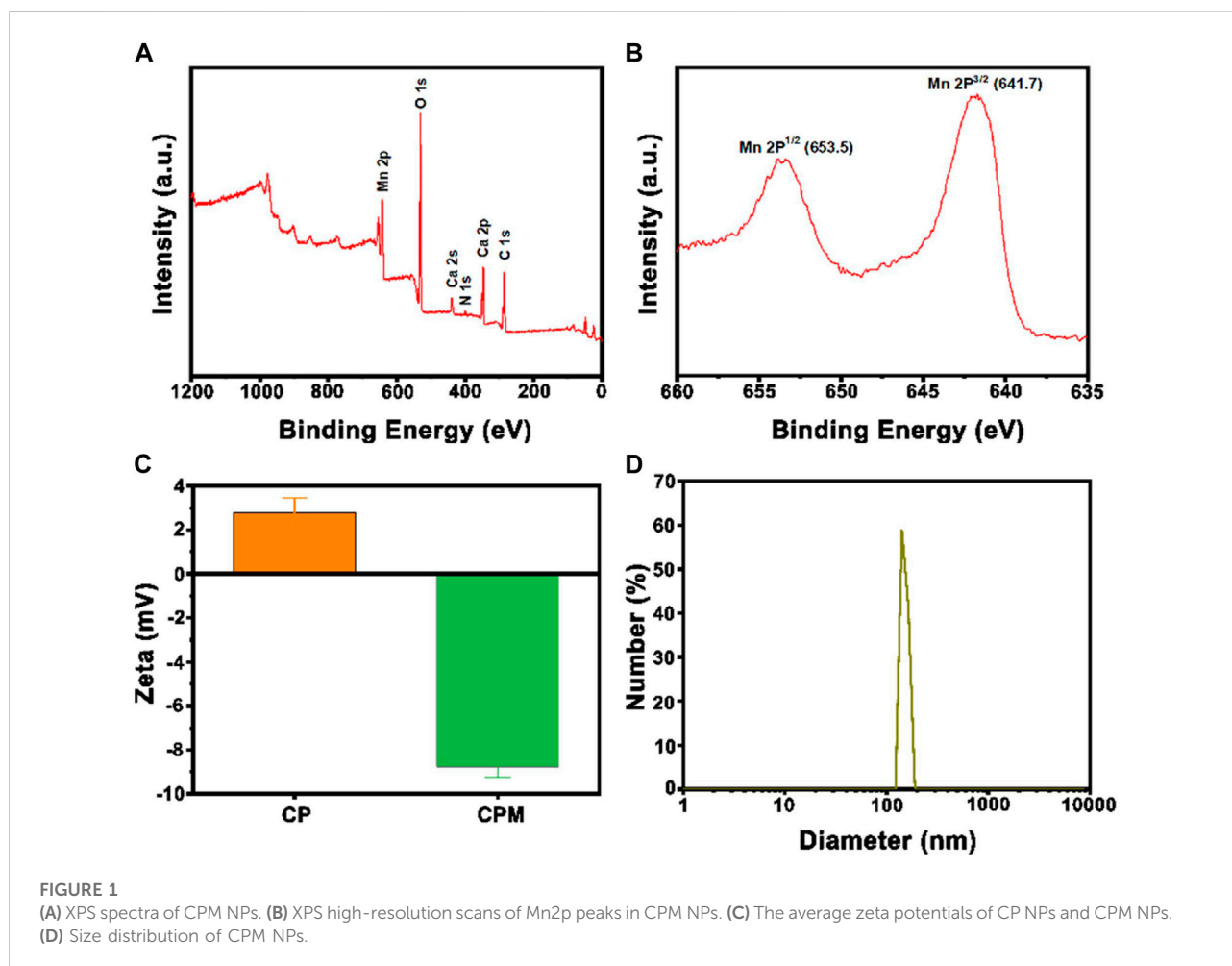
## Immunogenic cell death and dendritic cell maturation *in vitro*

To evaluate calreticulin (CRT) expression after various treatments, 4T1 cells were incubated with CPM NPs (20  $\mu\text{g ml}^{-1}$ ) for 12 h. After a treatment with a 1,064 nm laser (1  $\text{W cm}^{-2}$ , 5 min) and/or US (1.0 MHz, 20% duty cycle, 0.5  $\text{W cm}^{-2}$ , 2 min), the 4T1 cells were incubated with CRT antibodies (1:100; Abcam, EPR3924) for 30 min. After washing three times with PBS, Cy5-labeled goat anti-mouse IgG (H + L) (1:400, Abbkine, A23320) was added to the cells and incubated at 37°C for 2 h. Finally, CLSM was used to visualize the cells after staining with DAPI for 15 min. The release of ATP and HMGB1 was examined using the Chemiluminescence ATP Determination Kit (Solarbio, BC0300) and the HMGB1 enzyme-linked immunosorbent assay (ELISA) Kit (CUSABIO, CSB-E08225M). Briefly, 4T1 cells were incubated with 20  $\mu\text{g ml}^{-1}$  CPM NPs for 12 h. Then, after a treatment with a 1,064 nm laser (1  $\text{W cm}^{-2}$ , 5 min) and/or US (1.0 MHz, 20% duty cycle, 0.5  $\text{W cm}^{-2}$ , 2 min), the release level of HMGB1 in the cell culture medium was detected using an HMGB1 ELISA Kit. Similarly, the release of ATP was measured using an ATP ELISA kit. To determine DCs maturation, 4T1 cells were cultured with CPM NPs (20  $\mu\text{g ml}^{-1}$ ) for 12 h. After a 1,064 nm laser (1  $\text{W cm}^{-2}$ , 5 min) and/or US (1.0 MHz, 20% duty cycle, 0.5  $\text{W cm}^{-2}$ , 2 min) treatment, the supernatant in the 6-well plate of the 4T1 cells was added to the 6-well plates seeded with DC cells (derived from the bone marrow of BALB/c mice after stimulation with GM-CSF) and then cultivated for 24 h. The control group was cultured in a fresh medium. DCs were detected using flow cytometry after staining with anti-CD11c-PE (BioLegend, 117,308), anti-CD80-PE/Cy5.5 (Biolegend, 104,722), and anti-CD86-APC (BioLegend, 105,012).

## *In vivo* antitumor efficiency

When the primary tumor volume grew to approximately 80  $\text{mm}^3$ , BALB/c mice were randomly divided into five groups: PBS (100  $\mu\text{l}$ ), CPM (CPM: 100  $\mu\text{l}$ , 1  $\text{mg ml}^{-1}$ ), CPM + US (1.0 MHz, 20% duty cycle, 2  $\text{W cm}^{-2}$ , 2 min), CPM + L (1  $\text{W cm}^{-2}$ , 5 min), CPM + US + L, and were subcutaneously injected with four injections of CPM NPs or PBS on days 0, 2, 4, and 6. The temperature of the tumor area was recorded using an infrared thermal imager (FLIR E8). Tumor weight and volume were monitored on alternating days for 15 days. After treatment, the mice were euthanized by dislocation of cervical vertebra and all major organs and tissues were removed and stained with hematoxylin and eosin. To further investigate immune responses during photothermal and immune tumor therapy, tumor-draining lymph nodes, spleens, and tumors were collected after 15 days of treatment. To assess the maturity of DCs *in vivo*, single-cell suspensions obtained after lymph node grinding were stained with anti-CD11c-PE (BioLegend, 117,308), anti-CD80-PE/Cy5.5 (Biolegend, 104,722), and anti-CD86-APC (BioLegend, 105,012), and then were analyzed by flow





diffusion method according to a previous report with minor modifications (Dong et al., 2018). Then,  $\text{MnO}_2$  was introduced to the surface of the CP NPs by the reaction of  $\text{MnCl}_2$  and  $\text{NaOH}$  to form CPM NPs. TEM was used to investigate the morphology and size of the CPM NPs. As shown in Schemes 1B,C, the CPM NPs with irregular spherical shapes exhibited a size of  $\sim 150$  nm. This size is suitable for cellular uptake. The corresponding elemental mapping demonstrated the homogeneous elemental distributions of C, O, N, Ca, and Mn in the CPM NPs (Scheme 1D). XPS analysis also confirmed the presence of C, N, O, Ca, and Mn in the CPM-NPs (Figure 1A). Moreover, the characteristic peaks at 653.5 and 641.7 eV in the high-resolution Mn 2p spectrum correspond to the Mn (IV) 2p<sub>1/2</sub> and Mn (IV) 2p<sub>3/2</sub> spin-orbit peaks of  $\text{MnO}_2$ , respectively (Figure 1B), illustrating the successful synthesis of CPM NPs (Chen et al., 2015; Zhao et al., 2015; Liu J et al., 2021). We also measured the zeta potentials of the CP and CPM NPs. As shown in Figure 1C, CPM NPs exhibited a lower average zeta potential ( $-8.76$  mV) than CP NPs (2.79 mV). Negatively charged CPM NPs prolong blood circulation *in vivo*. To evaluate the dispersity of CPM NPs

in water, dynamic light scattering (DLS) was used to detect the hydrodynamic diameter of the CPM NPs. As illustrated in Figure 1D, the CPM NPs showed an average hydrodynamic diameter of  $\sim 150$  nm, demonstrating the superior dispersibility of CPM NPs in water. We further investigated the colloidal stability of CPM NPs by immersing CPM NPs in various solutions. After 7 days of immersion in water, phosphate-buffered saline (PBS, pH 7.4), FBS, and Medium, the digital photograph of CPM NPs did not display any obvious precipitation (Supplementary Figure S1). Homoplastically, the hydrodynamic diameter of CPM NPs showed non-significant change after immersion in water for a week (Supplementary Figure S2). These results clearly revealed the excellent stability of CPM NPs. Notably, CPM NPs were stable in the presence of excess FBS protein, suggesting that CPM NPs can be stable in the blood stream (Hwang et al., 2008).

As the bubble generation ability of CPM NPs is crucial for this therapeutic system, we evaluated its bubble generation ability carefully under various conditions in the following study. Theoretically, in a simulated tumor environment with slightly

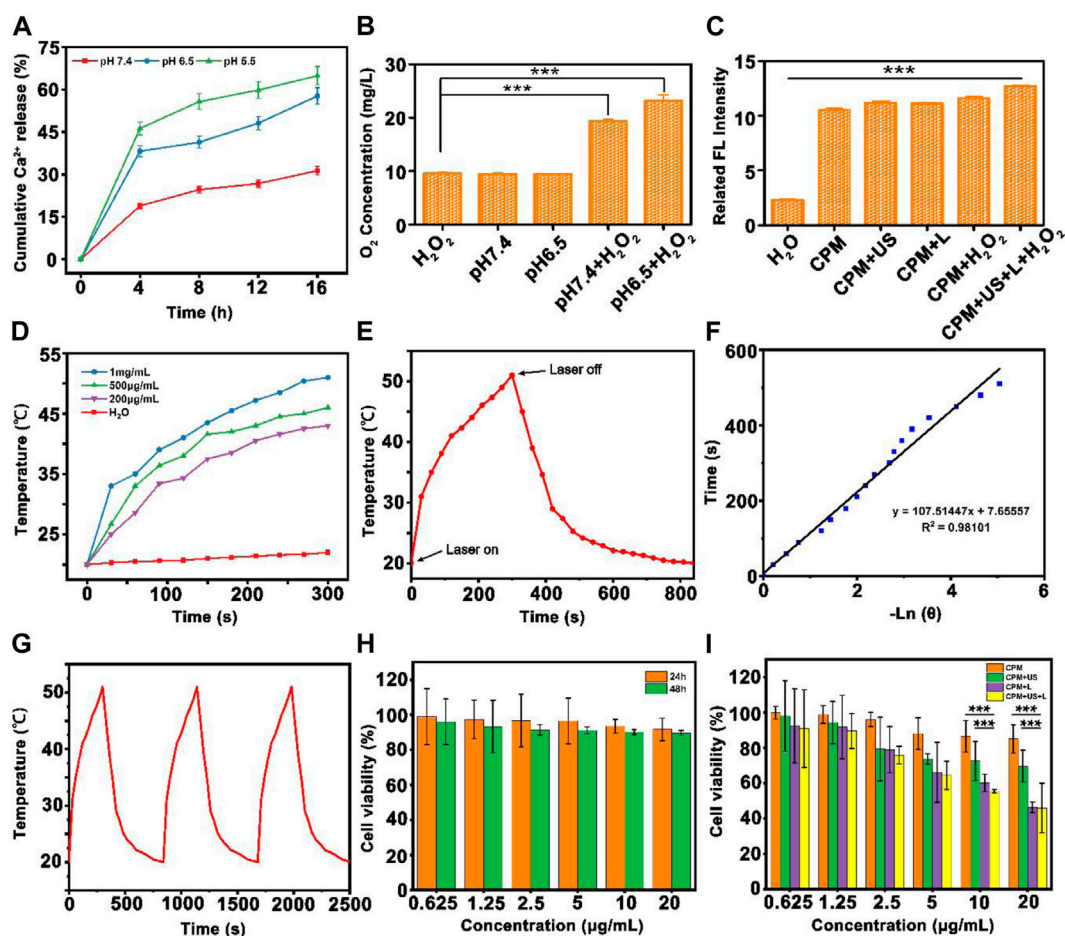


FIGURE 2

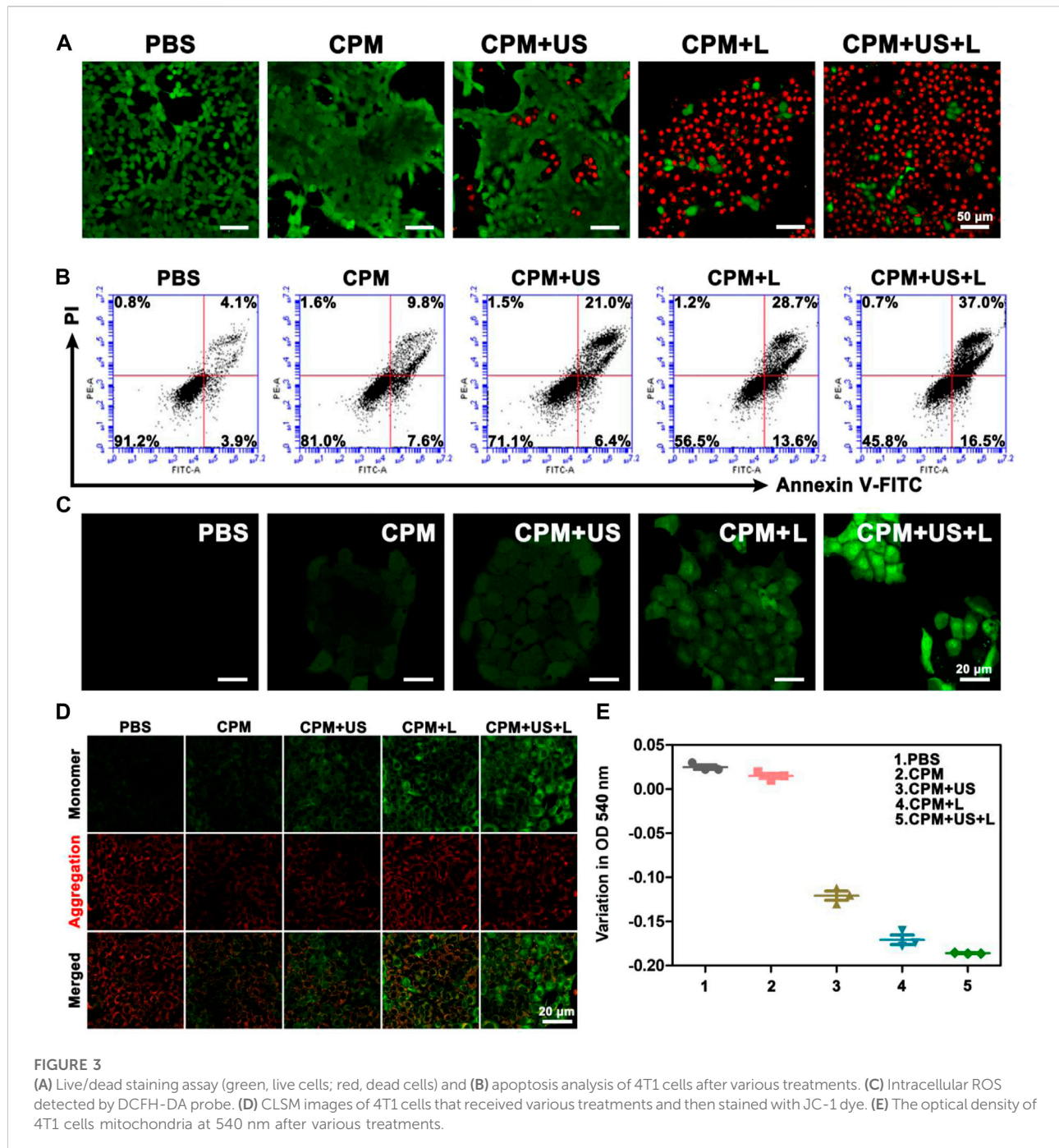
The physicochemical characterization of CPM NPs. (A) Time-dependent release profiles of  $\text{Ca}^{2+}$  from CPM NPs in PBS at different pH values 5.5, 6.5, and 7.4. The release percentages were calculated as the amount of release of  $\text{Ca}^{2+}$  from CPM NPs/the total amount of  $\text{Ca}^{2+}$  in CPM NPs. (B) The oxygen concentrations produced by CPM NPs at different pH values in  $\text{H}_2\text{O}_2$  solution ( $100 \mu\text{M}$ ). (C) SOSG fluorescence intensities of materials under different conditions. (D) Heating curves of different concentrations of CPM NPs under  $1,064 \text{ nm}$  laser irradiation. (E) Temperature record of CPM NPs ( $1 \text{ mg ml}^{-1}$ ) under laser irradiation. (F) Linear-time data versus  $-\ln(\theta)$  obtained from the cooling period of NIR laser off. (G) The photothermal conversion cycling test of CPM NPs ( $1 \text{ mg ml}^{-1}$ ) during three laser on/off cycles. (H) Viability of 293T after being treated with different concentrations of CPM NPs for 24 and 48 h. (I) Cell survival rate of 4T1 cells after being treated by different treatment groups.

acidic and high levels of hydrogen peroxide,  $\text{CaCO}_3$  nanoparticles can be decomposed to produce  $\text{CO}_2$  and  $\text{Ca}^{2+}$  by the following reaction:  $\text{CaCO}_3 + 2\text{H}^+ \rightarrow \text{CO}_2 + \text{Ca}^{2+} + \text{H}_2\text{O}$ . At the same time,  $\text{MnO}_2$  nanoparticles can be disintegrated to generate  $\text{O}_2$  and  $\text{Mn}^{2+}$  ions by the following reaction:  $\text{MnO}_2 + 2\text{H}^+ + \text{H}_2\text{O}_2 \rightarrow \text{Mn}^{2+} + 2\text{H}_2\text{O} + \text{O}_2$  (Sun et al., 2021). As shown in Supplementary Figure S3, both CP NPs and CPM NPs showed a certain bubble generating ability in pH 6.5 solutions with the existence of  $\text{H}_2\text{O}_2$ . The stimulation of laser or ultrasound promote the generation of bubbles both in CP NPs and CPM NPs. Obviously, the CPM + US + L +  $\text{H}_2\text{O}_2$  group produced the largest number of bubbles compared to the other groups. Hence, it is reasonable to speculate that the dual gas production of  $\text{O}_2$  and  $\text{CO}_2$  in CPM NPs solutions greatly contributes to the large

amounts of bubbles compared to CP NPs solution that only produces  $\text{CO}_2$ .

Since pH-responsive  $\text{Ca}^{2+}$  release from CPM NPs is crucial for the calcium-overload-induced cancer immune therapy, we evaluated the  $\text{Ca}^{2+}$  release ability at various pH (5.5, 6.5, and 7.4). As shown in Figure 2A, time-related release behavior of  $\text{Ca}^{2+}$  from CPM NPs was observed. CPM NPs in the pH 5.5 solutions showed the highest calcium release rate (65%) compared to the pH 7.4 (31%) and pH 6.5 (58%) solutions. These results demonstrate the pH-dependent release behavior of CPM NPs. Therefore, CPM NPs are promising for  $\text{Ca}^{2+}$ -induced immunotherapy.

As previously reported,  $\text{MnO}_2$  nanoparticles can trigger the decomposition of  $\text{H}_2\text{O}_2$  to produce oxygen and  $\text{Mn}^{2+}$  by



consuming  $H^+$  ions (Liu Y et al., 2019). Using a portable oxygen-dissolving apparatus, we further investigated the oxygen generation capability of CPM NPs at different pH with and without  $H_2O_2$  (100  $\mu M$ ). A similar oxygen content of approximately 10 mg/L was observed in the pure  $H_2O_2$  and PBS (pH 7.4) group (CPM NPs dissolved in pH 7.4 PBS solution) and the pH 6.5 group (and the CPM NPs dissolved in pH 6.5 PBS solution). When  $H_2O_2$  was added, the pH 7.4 +

$H_2O_2$  group exhibited significantly increased oxygen levels (~20 mg/L). Compared to the other groups, the pH 6.5 +  $H_2O_2$  group exhibited the highest oxygen content (~24 mg/L) (Figure 2B). These results demonstrated the potential of CPM to eliminate tumor hypoxia. Then, the ROS generation capability of CPM NPs in pH 6.5 solution under various conditions was investigated. The fluorescence intensity was clearly increased in the presence of CPM NPs under various treatments

compared to that in the pure H<sub>2</sub>O group (Figure 2C). However, the highest fluorescence intensity was obtained by the implementation of laser and ultrasound irradiation with H<sub>2</sub>O<sub>2</sub>. The above results show that laser and ultrasound irradiation can promote the production of ROS along with CPM NPs in the tumor microenvironment.

## ***In vitro* photothermal effect of calcium carbonate-polydopamine-manganese oxide nanoparticles**

As reported in previous studies, both PDA and MnO<sub>2</sub> exhibit excellent photothermal conversion capability (Farokhi et al., 2019; Liu Y et al., 2021), which inspired us to evaluate the photothermal properties of the CPM NPs. We examined the heating curves of CPM NPs at different concentrations under 1,064 nm laser irradiation (1,064 nm, 1 W cm<sup>-2</sup>). The CPM NPs exhibited both time- and concentration-dependent photothermal heating (Figure 2D). After 15 min of laser stimulation, the temperature of the CPM NPs with a concentration of 1 mg ml<sup>-1</sup> increased significantly from 20°C to 51°C while the temperature of the CPM NPs with a concentration of 200 µg ml<sup>-1</sup> increased to 43°C. Subsequently, we calculated the photothermal conversion efficiency of CPM NPs to be 26.31% (Figures 2E,F). As depicted in Figure 2G, no apparent temperature decrease was observed during the 1,064 nm laser irradiation for three on/off cycles, indicating the excellent photothermal stability of the CPM NPs.

## **Antitumor effects *in vitro***

To evaluate the combined antitumor photothermal and immunity effect *in vitro*, the cytotoxic effect of CPM NPs on tumor cells under various conditions was investigated. A low toxicity to normal cells is a necessary requirement for the application of CPM NPs in biological systems. We used normal human renal epithelial cells (293T) to evaluate the biosafety of CPM NPs by incubating the cells with different concentrations of CPM NPs for 24 or 48 h. It was found that the cell survival rate exceeded 90% even for incubation with the highest concentration (20 µg ml<sup>-1</sup>) for 48 h (Figure 2H), reflecting the excellent biocompatibility of CPM NPs. The antitumor effects of CPM NPs were further investigated. Various concentrations (0.625, 1.25, 2.5, 5, 10, and 20 µg ml<sup>-1</sup>) of CPM NPs were co-incubated with 4T1 cells and treated with 1,064 nm laser irradiation (1 W cm<sup>-2</sup>, 5 min) and US (1.0 MHz, 20% duty cycle, 0.5 W cm<sup>-2</sup>, 2 min). As shown in Figure 2I, the CPM group exhibited weak killing ability (85%) of 4T1 cells (20 µg ml<sup>-1</sup>) compared to the CPM + US (69.6%) and CPM + L groups (46.3%). The decreased cell viability of the CPM + US group may be attributed to the ultrasound-promoted calcium

overload. Hyperthermia triggered by the photothermal effect of CPM NPs under laser irradiation also promoted cell death. The CPM + US and CPM + L groups exhibited concentration-dependent cell viability. As expected, the 4T1 cells treated with CPM + US + L showed the highest cell lethality (45.9%), indicating the most severe cell damage.

To depict cell viability more intuitively, calcein-AM/PI was employed to conduct a living/dead assay by staining dead cells and living cells to red and green, respectively. As depicted in Figure 3A, only bright green fluorescence, representing live cells, appeared in the CPM and PBS groups, confirming the negligible killing effect. A few dead cells appeared in the CPM + US group, while more dead cells were observed in the CPM + L group, proving that the cytotoxic effect of photothermal therapy is better than that of ultrasound. As expected, the CPM + US + L group showed the highest number of dead cells compared to the other groups. This result was consistent with that of the MTT assay (Figure 2I). Additionally, we investigated the apoptosis induced by CPM NPs under various treatments. As shown in Figure 3B, the apoptosis rates in the CPM, CPM + US, and CPM + L groups were 17.4%, 27.4%, and 42.3%, respectively. Under the application of both laser and ultrasound irradiation, the CPM + US + L group showed the highest apoptosis rate (53.5%). These results are in agreement with those of the MTT and living/dead assays. The above results demonstrated the superior antitumor effect of CPM + US + L. Subsequently, a series of experiments were conducted to elucidate the therapeutic mechanism. Alleviating hypoxia in the tumor microenvironment is critical for tumor therapy. Therefore, we firstly detected the effect of CPM NPs for hypoxia remission in cells. Red fluorescence indicates cell hypoxia. As revealed in Supplementary Figure S4, almost no red fluorescence was exhibited in the normal environment with or without CPM NPs. Under hypoxia environment, the obvious red fluorescence signal appears without CPM NPs. In contrast, the CPM-treated cells only exhibited faint red fluorescence, proving the effective hypoxia remission. The generation of ROS in 4T1 cells was evaluated using a DCFH-DA probe, with green fluorescence as the ROS indicator. CPM-treated cells showed weak fluorescence, which may be ascribed to the ROS production during MnO<sub>2</sub>-induced CDT and mitochondrial Ca<sup>2+</sup> overload (Wang et al., 2019). When either laser or ultrasound irradiation was applied, CPM-treated cells showed stronger fluorescence intensity (Figure 3C), suggesting that both laser irradiation and ultrasound promoted ROS production. This result may be caused by ultrasound-enhanced mitochondrial Ca<sup>2+</sup> overload and laser-promoted CDT (Zhang et al., 2021). As anticipated, the CPM + US + L group showed the strongest green fluorescence compared to the CPM + US and CPM + L groups, suggesting the superiority of the combination therapy. Mitochondrial Ca<sup>2+</sup> overload can damage the mitochondria, triggering a decrease in the mitochondrial membrane potential. We further determined the degree of mitochondrial damage after various treatments using JC-1 (mitochondrial membrane potential probe). J-aggregates with red fluorescence and monomers with green fluorescence were found in normal and damaged mitochondrial membranes, respectively. As

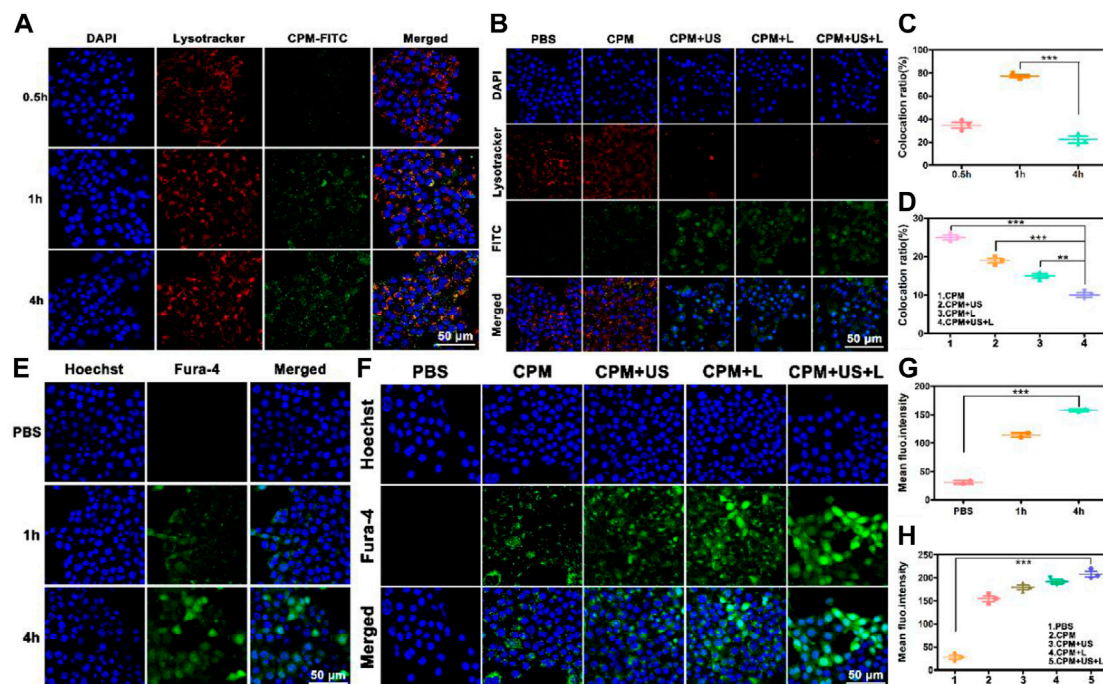


**FIGURE 4**

(A) The CLSM of CPM NPs (labeled with FITC,  $20 \mu\text{g ml}^{-1}$ ) with lysosomes in 4T1 cells after incubation with CPM NPs for 0.5, 1, and 4 h, respectively. (B) The CLSM of CPM NPs (labeled with FITC,  $20 \mu\text{g ml}^{-1}$ ) with lysosomes in 4T1 cells being various treatments. (C) The co-location ratio of CPM NPs with lysosomes in 4T1 cells after incubated with CPM for 0.5, 1, and 4 h, respectively. (D) The co-location ratio of CPM NPs with lysosomes in 4T1 cells after various treatments. (E) Confocal images of 4T1 cells incubated with CPM NPs ( $20 \mu\text{g ml}^{-1}$ ) at different time points and stained with an intracellular  $\text{Ca}^{2+}$  indicator, Fluo-4 AM ( $5 \mu\text{M}$ ). (F) Confocal images of 4T1 cells being various treatments after incubated with CPM NPs ( $20 \mu\text{g ml}^{-1}$ ) for 4 h and stained with an intracellular  $\text{Ca}^{2+}$  indicator, Fluo-4 AM ( $5 \mu\text{M}$ ). (G) Mean fluorescence intensity (MFI) of intracellular  $\text{Ca}^{2+}$  level in 4T1 cells. (H) MFI of intracellular  $\text{Ca}^{2+}$  level in 4T1 cells after various treatments.

shown in Figure 3D, weak green fluorescence appeared in the cells of the CPM group, confirming slight mitochondrial damage. The green fluorescence signal was enhanced under laser and ultrasound stimulation, indicating that the application of US and laser increased mitochondrial damage. As expected, the cells in the CPM + US + L group showed the strongest green fluorescence signal, suggesting that the combination of laser irradiation and ultrasound resulted in the most severe mitochondrial damage. In addition to decreased mitochondrial membrane potential, mitochondrial swelling is an important indicator of mitochondrial damage. Therefore, we performed a mitochondrial swelling assay to verify the mitochondrial damage. Normal mitochondria show strong ultraviolet-visible (UV-vis) absorption at 540 nm, whereas the absorbance at 540 nm decreases when mitochondria are damaged. As shown in Figure 3E, the absorbance values of the cells at 540 nm were significantly decreased after treatment with laser irradiation or ultrasound compared to the PBS and CPM groups, indicating that both laser irradiation and ultrasound can induce strong mitochondrial swelling. As anticipated, the CPM + US + L group exhibited the most obvious mitochondrial swelling, which was consistent with the results of the mitochondrial membrane potential assay.  $\text{Ca}^{2+}$  is considered a key factor in the regulation

of mitochondrial activity (Giorgi et al., 2018; Nemani et al., 2018; Rossi et al., 2019). This inspired us to explore whether mitochondrial damage was related to  $\text{Ca}^{2+}$  overload. First, we used FITC-labeled CPM NPs and red Lyso-Tracker to investigate the internalization and lysosomal escape of CPM NPs in 4T1 cells. As indicated in Figure 4A, the green fluorescence intensity of CPM-FITC gradually increased with prolonged co-culture time of CPM-FITC with 4T1 cells. Notably, when CPM-FITC was co-incubated with 4T1 cells for 4 h, the green fluorescence of CPM-FITC separated from the lysosomal red fluorescence was clearly observed unlike for those at 0.5 and 1 h. The co-localization rate of CPM-FITC fluorescence and lysosomal fluorescence was calculated using ImageJ analysis. As shown in Figure 4C, the colocalization rate of CPM-FITC fluorescence and lysosomal fluorescence reached 77% after 1 h incubation, but subsequently decreased to 22% after 4 h of incubation, confirming that CPM NPs underwent effective lysosomal escape. We then explored the internalization and lysosomal escape of 4T1 cells under various treatments after co-culture with CPM-FITC for 4 h. Compared to the CPM group, the green fluorescence of 4T1 cells was significantly enhanced after laser or ultrasound irradiation (Figure 4B), verifying that laser and ultrasound irradiation promoted the cellular uptake of CPM NPs.

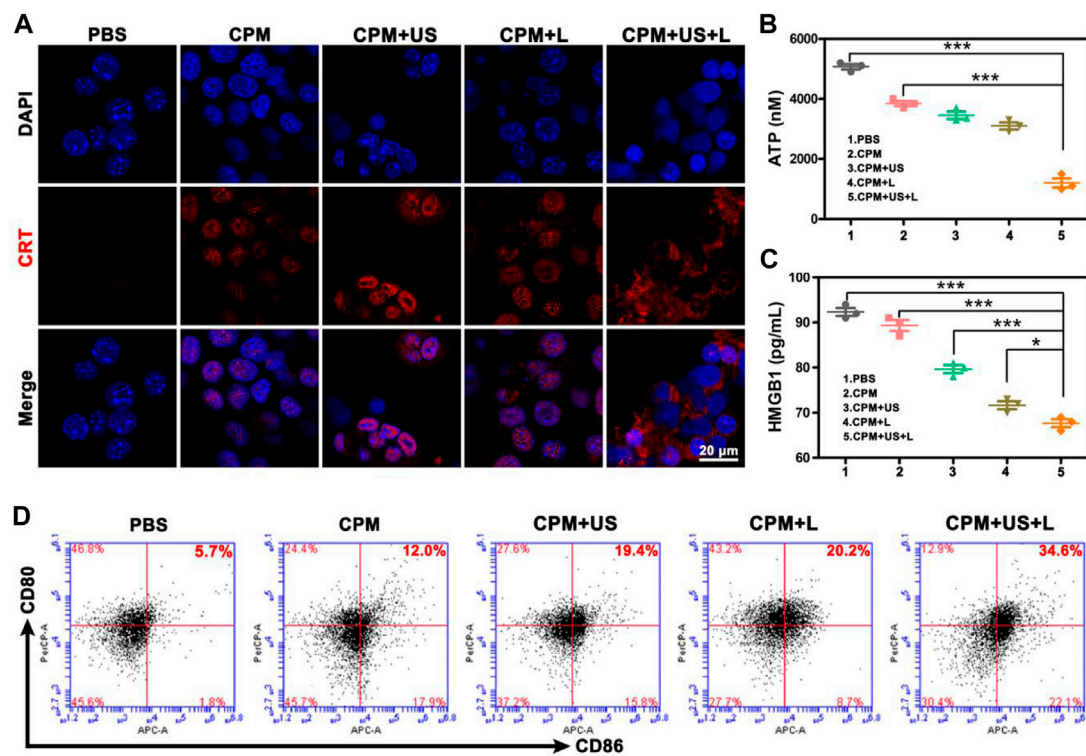


FIGURE 5

(A) CRT exposure. (B) Intracellular ATP and (C) HMGB1 release from 4T1 cells after various treatments. Data are means  $\pm$  SD. \* $p < 0.05$ , \*\* $p < 0.01$ , and \*\*\* $p < 0.001$ . (D) Flow cytometry analysis of the expression of CD80<sup>+</sup>/CD86<sup>+</sup> DC cells (markers for maturation) on the surface of DCs after various treatments.

This is attributed to the higher cell permeability caused by the photothermal effect and ultrasonic vibration, which facilitates the entry of nanoparticles into cells (Hu et al., 2020).

In addition, most of the separated green fluorescence was observed in the CPM + US + L group. As shown in Figure 4D, the fluorescence colocalization rates of CPM, CPM + US, CPM + L, and CPM + US + L groups were calculated to be 25%, 19%, 15%, and 10%, respectively. Notably, red fluorescence was significantly reduced in the CPM + US, CPM + L, and CPM + US + L groups, indicating strong lysosomal damage caused by the release of CPM NPs into the cytoplasm (Weyergang et al., 2014; Huang et al., 2019). These results demonstrated that laser and ultrasound irradiation accelerated lysosomal escape, and the combination treatment further promotes this process. Then, we detected the Ca<sup>2+</sup> uptake by CPM NPs after co-culture with 4T1 cells for 4 h. The green fluorescence of Fluo-4 AM was used as the Ca<sup>2+</sup> probe. The intracellular Ca<sup>2+</sup> fluorescence intensity increased in a time-dependent manner in 4T1 cells (Figures 4E,G). To study the effects of laser and ultrasound irradiation on intracellular Ca<sup>2+</sup> content, we treated 4T1 cells after culturing with CPM NPs for 4 h. As shown in Figure 4F, both the CPM + US and CPM + L groups exhibited brighter green fluorescence than the CPM group, proving that laser and

ultrasound irradiation facilitated Ca<sup>2+</sup> internalization by 4T1 cells. The strongest Ca<sup>2+</sup> fluorescence intensity in the CPM + US + L group confirmed the superiority of the combined laser and ultrasound treatment for Ca<sup>2+</sup> uptake. Moreover, quantitative analysis of the fluorescence intensity of Ca<sup>2+</sup> also proved this conclusion (Figure 4H). The above results indicate that CPM NPs under laser and ultrasound irradiation effectively increase intracellular Ca<sup>2+</sup> content, resulting in Ca<sup>2+</sup> overload and thereby inducing mitochondrial damage.

To assess the antitumor immune response to CPM NPs under various treatments, we explored ICD. The release of DAMPs from tumor cells is an important step in triggering ICD in tumor immunotherapy. During ICD, DAMPs, including CRT, ATP, and HMGB1, can be exposed to the membrane surface of tumor cells to facilitate DC maturation and stimulate optimal antigen presentation. Confocal microscopy was used to observe the level of CRT secretion on the surface of 4T1 cells after treatment, and the levels of intracellular ATP and HMGB1 release were determined using the ATP and HMGB1 ELISA kits, respectively. We found that CRT expression on the cell surface of the CPM group was enhanced compared to that in the PBS group, which may be caused by the Ca<sup>2+</sup>- and Mn<sup>2+</sup>-evoked ICD (Figure 5A). When laser or ultrasound irradiation was applied, a higher CRT exposure was observed. As

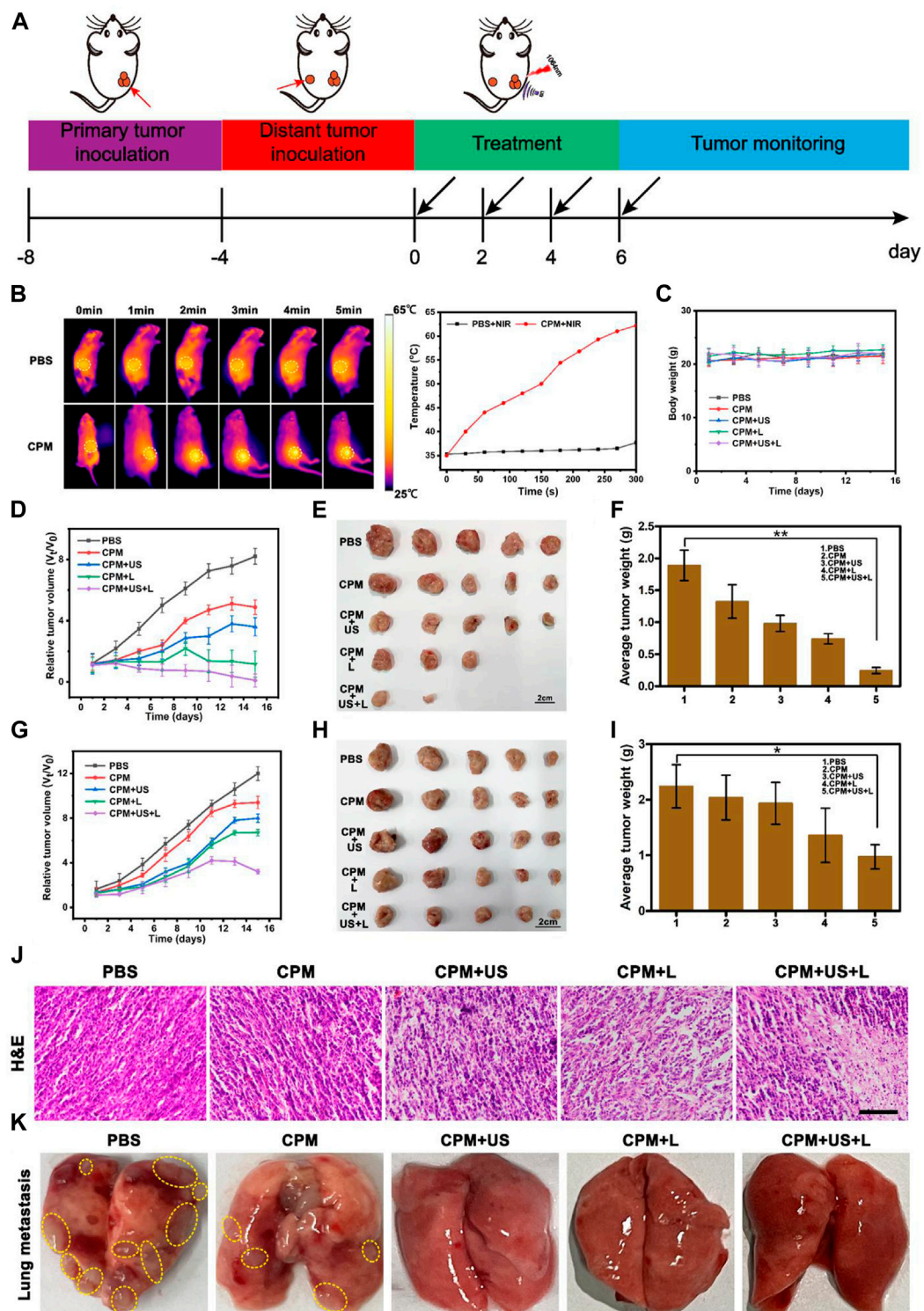


**FIGURE 6**  
**(A)** Schematic illustration of the animal tumor model and treatment process. **(B)** Infrared thermographic images of mice in PBS + NIR and CPM + NIR groups and the corresponding temperatures curves of mice. (1,064 nm, 1 W cm<sup>-2</sup>, 5 min). **(C)** Average body weight curves during treatment. **(D)** Relative tumor volumes-time curves of 4T1 primary tumors in mice after various treatments. **(E)** Representative tumor pictures of 4T1 primary tumor and **(F)** average tumor weights obtained on the 15th day. **(G)** Relative tumor volumes-time curve of 4T1 distant tumors in mice after various treatments. **(H)** Representative tumor pictures of 4T1 distant tumor and **(I)** average tumor weights obtained on the 15th day. Data are means ± SD, \**p* < 0.05. **(J)** H and E staining images of primary tumors tissues. (Scale bar: 100 μm). **(K)** Representative photographs of lung tissues after various treatments.

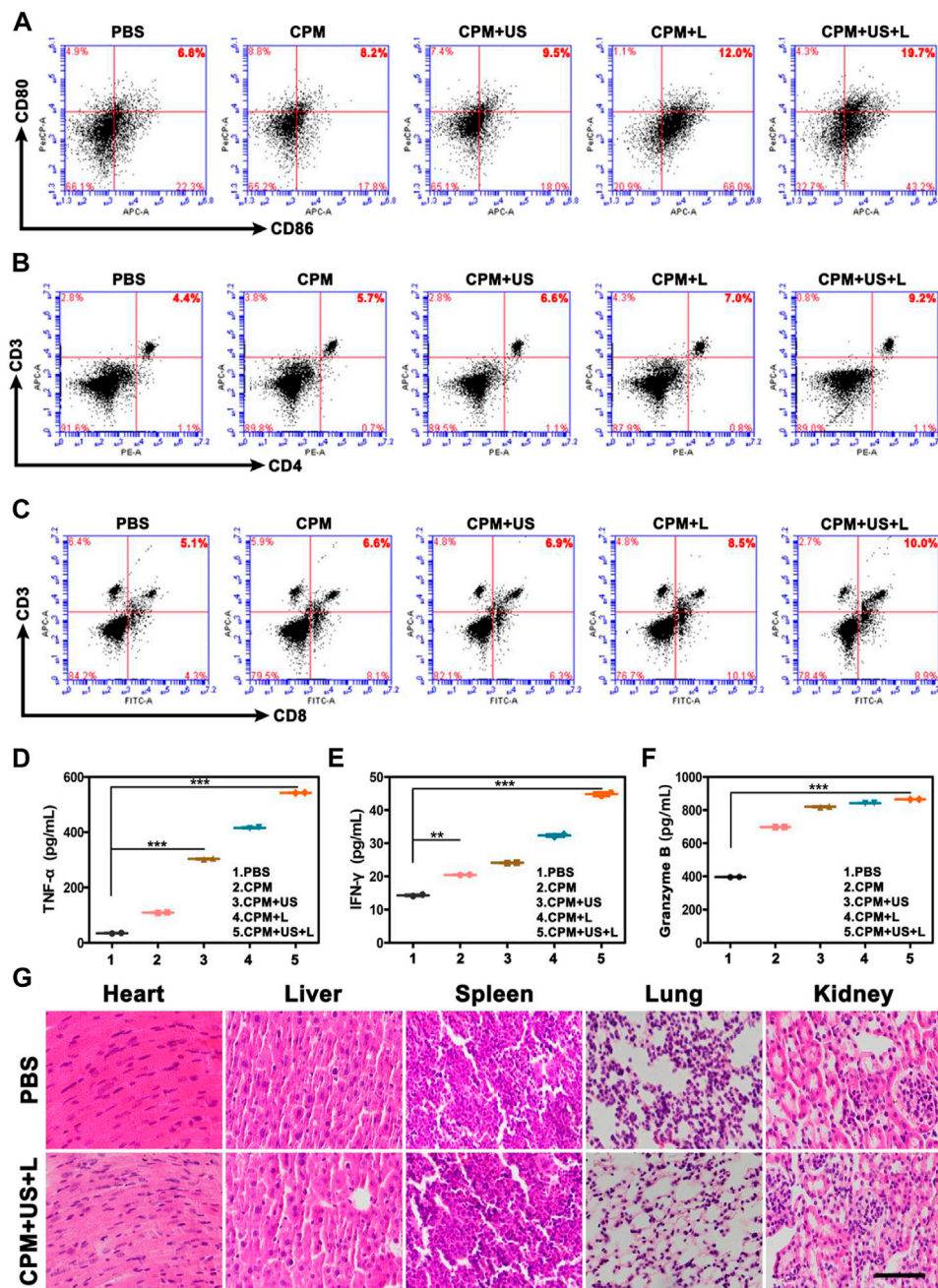


**FIGURE 7** Representative flow cytometry profiles of (A) CD80<sup>+</sup>/CD86<sup>+</sup> DC cells after indicated procedures in the lymph nodes, (B) CD3<sup>+</sup>/CD4<sup>+</sup> T cells in the spleen and (C) CD3<sup>+</sup>/CD8<sup>+</sup> T cells in the spleen. (D–F) The ELISA analysis of intraserosus cytokine levels of TNF-α, IFN-γ, and Granzyme B after different treatments on day 15. (G) H and E-stained images of major organs of BALB/c mice in various groups. (Scale bar: 100 μm).

expected, the CPM + US + L group showed the highest CRT exposure, demonstrating that the laser and ultrasound irradiation promoted immune responses. HMGB1 and ATP have been identified as other ICD biomarkers in 4T1 cells. As illustrated in Figures 5B,C, the intracellular release of HMGB1 and ATP significantly decreased in the CPM + US + L, CPM + US, and

CPM + L groups compared to the PBS and CPM groups. Among these, CPM + US + L exhibited the most significant decrease. These results confirmed that CPM + US and CPM + L can trigger an effective ICD that was further promoted by the combination of laser and ultrasound irradiation. Numerous studies have demonstrated that DAMPs released from necrotic or apoptotic tumor cells can

stimulate DCs maturation. DCs maturation was measured using flow cytometry. The mean percentage of mature DCs in the CPM + US + L group (34.6%) was significantly higher than that in the PBS (5.7%), CPM (12.0%), CPM + US (19.4%), and CPM + L (20.2%) groups (Figure 5D). These results verified that laser and ultrasound irradiation with CPM NPs can effectively induce ICD and promote DC maturation, thereby activating the antitumor immune response.

## ***In vivo* synergistic photothermal therapy and immune therapy**

Tumor therapy *in vivo* strictly followed the experimental scheme (Figure 6A). First, the therapeutic efficiency of the treatment system for primary and distant tumors was assessed simultaneously using a bilateral 4T1 tumor model. Different numbers of 4T1 cells ( $2 \times 10^6$  cells per mouse and  $1 \times 10^6$  cells per mouse) were inoculated into both the right (defined as the primary tumor) and left (defined as the distant tumor) flank regions of BALB/c mice on days -8 and -4, respectively. CPM NPs (100  $\mu$ l, 1 mg ml<sup>-1</sup>) were injected into the primary tumor region of BALB/c mice prior to each irradiation of the BALB/c primary tumors with 1,064 nm laser (1 W cm<sup>-2</sup>, 5 min) or US (1.0 MHz, 20% duty cycle, 2 W cm<sup>-2</sup>, 2 min). First, the photothermal effect of the laser-irradiated BALB/c mice was assessed using an infrared thermal imaging camera. After the injection of PBS or CPM NPs, mouse tumor areas were irradiated with a 1,064 nm laser (1 W cm<sup>-2</sup>), and temperature changes were recorded every 30 s using an infrared camera. Photothermal photographs of the mice showed that the CPM group exhibited time-dependent heating. The temperature of the CPM group increased from 35 to 62.2°C after 5 min of laser irradiation, showing a strong photothermal performance (Figure 6B). By contrast, the temperature for the PBS group only increased by 2.4°C within 5 min of laser exposure. Body weight changes (Figure 6C) and tumor volumes of each mouse were measured every 2 days. The relative volume curves of the tumors (including primary and distant tumors) were plotted according to the records. After 15 days of treatment, the mice were euthanized by dislocation of cervical vertebra and the primary and distant tumors were imaged and weighed. Unlike the malignant proliferation of 4T1 cells in the PBS group, the CPM + US and CPM + L groups showed significant inhibitory effects on tumor growth; notably, the inhibition of tumor growth was most pronounced in the CPM + US + L group (Figure 6D). The tumor images and weights showed the same trend (Figures 6E,F). These results suggest that the combination of photothermal therapy and immunity can significantly inhibit tumor growth, which is consistent with its outstanding antitumor effect *in vitro*. As expected, the growth of distant tumors in mice exhibited the same trend

as the growth of the primary tumor. Notably, the CPM + US + L group displayed obvious inhibition compared to the other groups (Figures 6G–I). Histological analysis of the primary tumor was performed to detect tissue damage. As illustrated in Figure 6J, after different treatments, different degrees of apoptosis in tumor cells with shrunken and broken nuclei were observed. The CPM + US and CPM + L groups exhibited more severe apoptosis than the CPM and PBS groups. It is important to note that CPM + US + L showed the greatest tumor cell damage, further confirming the antitumor efficacy of the different treatments.

## ***In vivo* anti-lung metastasis ability and immunity of synergistic photothermal therapy and immune therapy**

To comprehensively evaluate the antitumor ability of CPM, we also investigated the anti-lung metastasis ability of CPM *in vivo*. As shown in Figure 6K, the lungs of the mice in the PBS group exhibited a large number of pulmonary nodules that were significantly reduced in the CPM group. Additionally, the lung surfaces of the mice in the CPM + US, CPM + L, and CPM + US + L groups were flat, further demonstrating the superior antitumor metastasis ability of this therapeutic platform.

After the ability of CPM NPs to induce ICD and facilitate DC cell maturation was verified *in vitro*, we further investigated the antitumor immune responses of CPM NPs after various treatments *in vivo*. Flow cytometry was used to determine the DCs maturation (CD11c<sup>+</sup>/CD80<sup>+</sup>/CD86<sup>+</sup>) levels in the draining lymph nodes. As expected, the highest secretion level of DCs maturation (19.7%) was observed in the CPM + US + L group compared to the CPM (8.2%), CPM + US (9.5%), and CPM + L (12%) groups (Figure 7A), indicating that the combined laser and ultrasound therapy with CPM NPs effectively induced DCs maturation and improved the immune response *in vivo*. In addition, CD4<sup>+</sup> and CD8<sup>+</sup> T lymphocytes in the spleen were detected using flow cytometry. As shown in Figures 7B,C, the CPM + US + L group exhibited the strongest T cell-mediated immune response (CD4<sup>+</sup>/CD8<sup>+</sup> T cells: 9.2% and 10%) compared to the PBS (4.4% and 5.1%), CPM (5.7% and 6.6%), CPM + US (6.6% and 6.9%), and CPM + L (7.0% and 8.5%) groups, suggesting that combined treatment with CPM NPs promotes CD4<sup>+</sup> and CD8<sup>+</sup> T lymphocyte proliferation and infiltration. Subsequently, immune-mediated tumor killing was assessed by determining the levels of typical immune-related pro-inflammatory cytokines secreted by mature DC. The levels of cytokines TNF- $\alpha$ , IFN- $\gamma$ , and granzyme B in mouse serum were measured by enzyme-linked immunosorbent assay. As illustrated in Figures 7D–F, the highest cytokine levels

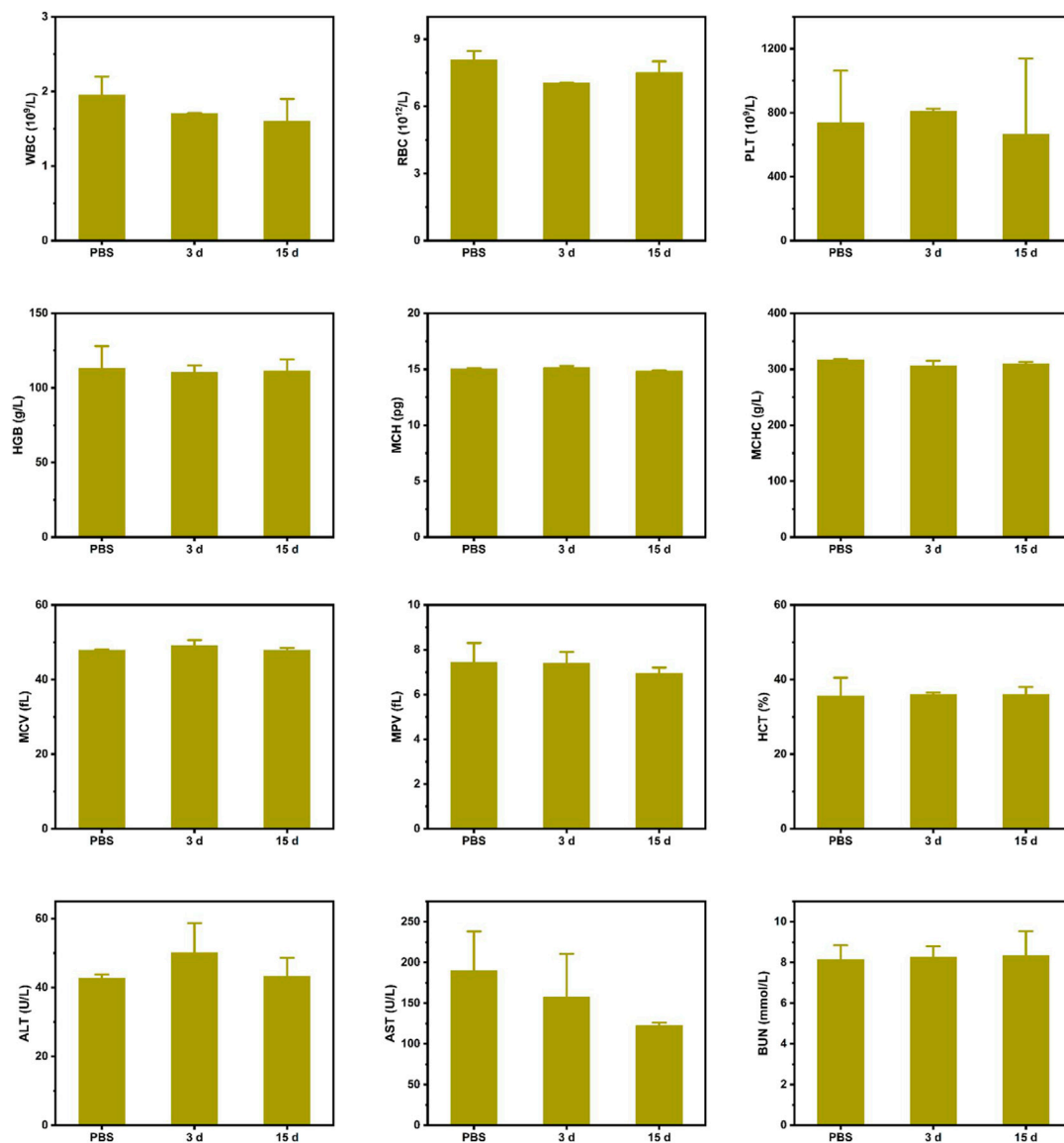


FIGURE 8

Major blood routine indexes, liver and kidney function indexes of mice after various treatments.

were found in the CPM + US + L group. Furthermore, the immune cell response against the tumor was also evaluated by immunohistochemistry analysis of tumor sections from mice. As expected, the highest proportion of CD4<sup>+</sup> and CD8<sup>+</sup> T cell infiltration in the tumor tissues were found in the CPM + US + L group (Supplementary Figure S4), suggesting that the combination of laser and ultrasound treatment could further promote the infiltration and proliferation of CD4<sup>+</sup> and CD8<sup>+</sup> T cells. These results indicated that the regimen of the combination photothermal and immune tumor therapy significantly enhanced the antitumor immune response.

## Systemic toxicity evaluation

Furthermore, to assess the biosafety of CPM, we performed histological analysis of major organs, including the heart, liver, spleen, lungs, and kidneys. As shown in Figure 7G, H and E-stained images of organ sections from the different treatment groups showed negligible abnormalities. Furthermore, the mice did not experience significant weight loss during the treatment period (Figure 6C), indicating the excellent biocompatibility of CPM NPs and the safety of the combined treatment procedure. Moreover, the functional indicators of the blood samples in the

CPM + US + L group were tested to assess the potential toxicity of CPM *in vivo*. As shown in Figure 8, compared to the PBS group, the CPM + US + L group showed negligible abnormalities in the relevant functional indicators on day 3 and at the end of treatment. The routine blood indices in the CPM + US + L group were found to be normal compared to those in the PBS group, indicating that no significant systemic infection or inflammation appeared during the entire evaluation period. The measured parameters, including alanine aminotransferase (ALT), aspartate aminotransferase (AST), and urea nitrogen (BUN), were within the normal range, indicating that the nanoparticles exhibited little toxicity to the liver. These results demonstrated the excellent compatibility and negligible adverse effects of the CPM + US + L treatment on the organism.

## Conclusion

In summary, a combined photothermal and immune tumor therapy platform was fabricated based on dual-gas nanogenerators (CPM NPs). The CPM NPs underwent responsive degradation in the tumor, resulting in the generation of  $\text{Ca}^{2+}$ ,  $\text{Mn}^{2+}$ ,  $\text{CO}_2$ , and  $\text{O}_2$ .  $\text{Ca}^{2+}$  and  $\text{Mn}^{2+}$  act as immune adjuvants that trigger ICD for immunotherapy. The relieved tumor hypoxia and cancer cell membrane rupture caused by sudden burst of bubbles ( $\text{CO}_2$  and  $\text{O}_2$ ) all contributed to ICD. The application of laser and ultrasound promoted the  $\text{Ca}^{2+}$  overload in mitochondria and explosion of  $\text{CO}_2$  and  $\text{O}_2$  bubbles by photothermal effects and ultrasonic waves thus improved immunotherapy effect. Superior PTT and immune synergistic therapeutic capabilities were demonstrated in both *in vitro* and *in vivo* experiments. Thus, this strategy based on CPM NPs dual-gas nano-generators is promising for future clinical cancer treatment.

## Data availability statement

The original contributions presented in the study are included in the article/Supplementary Material, further inquiries can be directed to the corresponding authors.

## Ethics statement

The animal study was reviewed and approved by Binzhou Medical University Animal Ethics Committee.

## Author contributions

XYL and YG, Data curation, Project administration, Writing-original draft. XZL and XH, Investigation, Project administration. YL and JS, Project administration. PW, HW, and HK, Project administration. MR, Conceptualization, Project administration. Writing-review and editing. SX, Resources, Funding acquisition, Writing-review and editing. RW, Conceptualization, Funding acquisition, Writing-review and editing. All authors read and approved the final manuscript.

## Funding

This work was supported by the National Natural Science Foundation of China (Grant Numbers 51903015 and 81772281), Science Fund of Shandong Laboratory of Advanced Materials and Green Manufacturing (Yantai) (AMGM 2021F03), and Shandong Science and Technology Committee (No. ZR2019MH022, ZR2020KH015), the Scientific Research Foundation of Binzhou Medical University (Project No. 50012304274), and Shandong Province Taishan Scholar Project (No. ts201712067), and Hong Kong RGC (GRF# 16308818, 16309920 and 16309421).

## Conflict of interest

The authors declare that the research was conducted in the absence of any commercial or financial relationships that could be construed as a potential conflict of interest.

## Publisher's note

All claims expressed in this article are solely those of the authors and do not necessarily represent those of their affiliated organizations, or those of the publisher, the editors and the reviewers. Any product that may be evaluated in this article, or claim that may be made by its manufacturer, is not guaranteed or endorsed by the publisher.

## Supplementary material

The Supplementary Material for this article can be found online at: <https://www.frontiersin.org/articles/10.3389/fbioe.2022.1005520/full#supplementary-material>

## References

- Chao, Y., Xu, L., Liang, C., Feng, L., Xu, J., Dong, Z., et al. (2018). Combined local immunostimulatory radioisotope therapy and systemic immune checkpoint blockade imparts potent antitumor responses. *Nat. Biomed. Eng.* 2 (8), 611–621. doi:10.1038/s41551-018-0262-6
- Chattopadhyay, S., Liu, Y. H., Fang, Z. S., Lin, C. L., Lin, J. C., Yao, B. Y., et al. (2020). Synthetic immunogenic cell death mediated by intracellular delivery of STING agonist nanoshells enhances anticancer chemo-immunotherapy. *Nano Lett.* 20 (4), 2246–2256. doi:10.1021/acs.nanolett.9b04094
- Chen Q, Q., Liu, L., Lu, Y., Chen, X., Zhang, Y., Zhou, W., et al. (2019). Tumor microenvironment-triggered aggregated magnetic nanoparticles for reinforced image-guided immunogenic chemotherapy. *Adv. Sci.* 6 (6), 1802134. doi:10.1002/advs.201802134
- Chen, Y., Ai, W., Guo, X., Li, Y., Ma, Y., Chen, L., et al. (2019). Mitochondria-targeted polydopamine nanocomposite with AIE photosensitizer for image-guided photodynamic and photothermal tumor ablation. *Small* 15 (30), e1902352. doi:10.1002/sml.201902352
- Chen, Y., Qin, W., Fan, R., Wang, J., and Chen, B. (2015). Hydrothermal synthesis and electrochemical properties of spherical  $\alpha$ -MnO<sub>2</sub> for supercapacitors. *J. Nanosci. Nanotechnol.* 15 (12), 9760–9765. doi:10.1166/jnn.2015.10490
- Dai, Y., Zhao, H., He, K., Du, W., Kong, Y., Wang, Z., et al. (2021). NIR-II excitation phototheranostic nanomedicine for fluorescence/photoacoustic tumor imaging and targeted photothermal-photonic thermodynamic therapy. *Small* 17 (42), e2102527. doi:10.1002/sml.202102527
- Deng, H., Zhou, Z., Yang, W., Lin, L. S., Wang, S., Niu, G., et al. (2020). Endoplasmic reticulum targeting to amplify immunogenic cell death for cancer immunotherapy. *Nano Lett.* 20 (3), 1928–1933. doi:10.1021/acs.nanolett.9b05210
- Ding, B., Zheng, P., Jiang, F., Zhao, Y., Wang, M., Chang, M., et al. (2020). MnOx nanospikes as nanoadjuvants and immunogenic cell death drugs with enhanced antitumor immunity and antimetastatic effect. *Angew. Chem. Int. Ed.* 59 (38), 16381–16384. doi:10.1002/anie.202005111
- Dong, Z., Feng, L., Hao, Y., Chen, M., Gao, M., Chao, Y., et al. (2018). Synthesis of hollow biomimeticized CaCO<sub>3</sub>-polydopamine nanoparticles for multimodal imaging-guided cancer photodynamic therapy with reduced skin photosensitivity. *J. Am. Chem. Soc.* 140 (6), 2165–2178. doi:10.1021/jacs.7b11036
- Duan, H., Guo, H., Zhang, R., Wang, F., Liu, Z., Ge, M., et al. (2020). Two-dimensional silicene composite nanosheets enable exogenous/endogenous-responsive and synergistic hyperthermia-augmented catalytic tumor theranostics. *Biomaterials* 256, 120206. doi:10.1016/j.biomaterials.2020.120206
- Duan, X., Chan, C., and Lin, W. (2019). Nanoparticle-mediated immunogenic cell death enables and potentiates cancer immunotherapy. *Angew. Chem. Int. Ed.* 58 (3), 670–680. doi:10.1002/anie.201804882
- Fan, W., Bu, W., Shen, B., He, Q., Cui, Z., Liu, Y., et al. (2015). Intelligent MnO<sub>2</sub> nanosheets anchored with upconversion nanoprobes for concurrent PH/H<sub>2</sub>O<sub>2</sub>-responsive UCL imaging and oxygen-elevated synergetic therapy. *Adv. Mat.* 27 (28), 4155–4161. doi:10.1002/adma.201405141
- Farokhi, M., Mottaghtalab, F., Saeb, M. R., and Thomas, S. (2019). Functionalized theranostic nanocarriers with bio-inspired polydopamine for tumor imaging and chemo-photothermal therapy. *J. Control. Release* 309, 203–219. doi:10.1016/j.jconrel.2019.07.036
- Feng, Q., Zhang, W., Yang, X., Li, Y., Hao, Y., Zhang, H., et al. (2018). pH/ultrasound dual-responsive gas generator for ultrasound imaging-guided therapeutic inertial cavitation and sonodynamic therapy. *Adv. Healthc. Mat.* 7 (5), 1700957. doi:10.1002/adhm.201700957
- Giorgi, C., Marchi, S., and Pinton, P. (2018). The machineries, regulation and cellular functions of mitochondrial calcium. *Nat. Rev. Mol. Cell Biol.* 19 (11), 713–730. doi:10.1038/s41580-018-0052-8
- Hu, Q., Huang, Z., Duan, Y., Fu, Z., and Liu, B. (2020). Reprogramming tumor microenvironment with photothermal therapy. *Bioconjug. Chem.* 31 (5), 1268–1278. doi:10.1021/acs.bioconjchem.0c00135
- Huang, X., Wu, J., He, M., Hou, X., Wang, Y., Cai, X., et al. (2019). Combined cancer chemo-photodynamic and photothermal therapy based on ICG/PDA/TPZ-Loaded nanoparticles. *Mol. Pharm.* 16 (5), 2172–2183. doi:10.1021/acs.molpharmaceut.9b00119
- Hwang, H. Y., Kim, I. S., Kwon, I. C., and Kim, Y. H. (2008). Tumor targetability and antitumor effect of docetaxel-loaded hydrophobically modified glycol chitosan nanoparticles. *J. Control. Release* 128 (1), 23–31. doi:10.1016/j.jconrel.2008.02.003
- Jeon, J., Yoon, B., Song, S. H., Um, W., Song, Y., Lee, J., et al. (2022). Chemiluminescence resonance energy transfer-based immunostimulatory nanoparticles for sonoimmunotherapy. *Biomaterials* 283, 121466. doi:10.1016/j.biomaterials.2022.121466
- Jiao, X., Sun, L., Zhang, W., Ren, J., Zhang, L., Cao, Y., et al. (2021). Engineering oxygen-deficient ZrO<sub>2</sub>-x nanoplateform as therapy-activated "immunogenic cell death (ICD)" inducer to synergize photothermal-augmented sonodynamic tumor elimination in NIR-II biological window. *Biomaterials* 272 120787. doi:10.1016/j.biomaterials.2021.120787
- Li, B., Gong, T., Xu, N., Cui, F., Yuan, B., Yuan, Q., et al. (2020). Improved stability and photothermal performance of polydopamine-modified Fe<sub>3</sub>O<sub>4</sub> nanocomposites for highly efficient magnetic resonance imaging-guided photothermal therapy. *Small* 16 (45), e2003969. doi:10.1002/sml.202003969
- Li, J., and Kataoka, K. (2021). Chemo-physical strategies to advance the *in vivo* functionality of targeted nanomedicine: The next generation. *J. Am. Chem. Soc.* 143 (2), 538–559. doi:10.1021/jacs.0c09029
- Li, X., Peng, X. H., Zheng, B. D., Tang, J., Zhao, Y., Zheng, B. Y., et al. (2018). New application of phthalocyanine molecules: From photodynamic therapy to photothermal therapy by means of structural regulation rather than formation of aggregates. *Chem. Sci.* 9 (8), 2098–2104. doi:10.1039/c7sc05115h
- Liu, J., Feng, L., and Wu, Y. (2021). Enzymatically synthesised MnO<sub>2</sub> nanoparticles for efficient near-infrared photothermal therapy and dual-responsive magnetic resonance imaging. *Nanoscale* 13 (25), 11093–11103. doi:10.1039/d1nr02400k
- Liu, J., Zhang, R., and Xu, Z. P. (2019). Nanoparticle-based nanomedicines to promote cancer immunotherapy: Recent advances and future directions. *Small* 15 (32), e1900262. doi:10.1002/sml.201900262
- Liu, P., Zhao, L., Pol, J., Levesque, S., Petrazzuolo, A., Pfirschke, C., et al. (2019). Crizotinib-induced immunogenic cell death in non-small cell lung cancer. *Nat. Commun.* 10 (1), 1486. doi:10.1038/s41467-019-09415-3
- Liu, Y., Pan, Y., Cao, W., Xia, F., Liu, B., Niu, J., et al. (2019). A tumor microenvironment responsive biodegradable CaCO<sub>3</sub>/MnO<sub>2</sub>-based nanoplateform for the enhanced photodynamic therapy and improved PD-L1 immunotherapy. *Theranostics* 9 (23), 6867–6884. doi:10.7150/thno.37586
- Liu, Y., Yu, B., Dai, X., Zhao, N., and Xu, F. J. (2021). Biomimeticized calcium carbonate nanohybrids for mild photothermal heating-enhanced gene therapy. *Biomaterials* 274, 120885. doi:10.1016/j.biomaterials.2021.120885
- Lv, M., Chen, M., Zhang, R., Zhang, W., Wang, C., Zhang, Y., et al. (2020). Manganese is critical for antitumor immune responses via cGAS-STING and improves the efficacy of clinical immunotherapy. *Cell Res.* 30 (11), 966–979. doi:10.1038/s41422-020-00395-4
- Lv, W., Cao, M., Liu, J., Hei, Y., and Bai, J. (2021). Tumor microenvironment-responsive nanozymes achieve photothermal-enhanced multiple catalysis against tumor hypoxia. *Acta Biomater.* 135, 617–627. doi:10.1016/j.actbio.2021.08.015
- Meng, X., Zhang, J., Sun, Z., Zhou, L., Deng, G., Li, S., et al. (2018). Hypoxia-triggered single-molecule probe for high-contrast NIR II/PA tumor imaging and robust photothermal therapy. *Theranostics* 8 (21), 6025–6034. doi:10.7150/thno.26607
- Nam, G. H., Lee, E. J., Kim, Y. K., Hong, Y., Choi, Y., Ryu, M. J., et al. (2018). Combined rho-kinase inhibition and immunogenic cell death triggers and propagates immunity against cancer. *Nat. Commun.* 9 (1), 2165. doi:10.1038/s41467-018-04607-9
- Nemani, N., Shanmughapriya, S., and Madesh, M. (2018). Molecular regulation of MCU: Implications in physiology and disease. *Cell Calcium* 74, 86–93. doi:10.1016/j.ceca.2018.06.006
- Park, J., Fan, Z., Kumon, R. E., El-Sayed, M. E., and Deng, C. X. (2010). Modulation of intracellular Ca<sup>2+</sup> concentration in brain microvascular endothelial cells *in vitro* by acoustic cavitation. *Ultrasound Med. Biol.* 36 (7), 1176–1187. doi:10.1016/j.ultrasmedbio.2010.04.006
- Parvizi, J., Parpura, V., Greenleaf, J. F., and Bolander, M. E. (2002). Calcium signaling is required for ultrasound-stimulated aggrecan synthesis by rat chondrocytes. *J. Orthop. Res.* 20 (1), 51–57. doi:10.1016/S0736-0266(01)00069-9
- Riera-Domingo, C., Audigé, A., Granja, S., Cheng, W. C., Ho, P. C., Baltazar, F., et al. (2020). Immunity, Hypoxia, and Metabolism—the Ménage à Trois of Cancer: Implications for Immunotherapy. *Physiol. Rev.* 100 (1), 1–102. doi:10.1152/physrev.00018.2019
- Rossi, A., Pizzo, P., and Filadi, R. (2019). Calcium, mitochondria and cell metabolism: A functional triangle in bioenergetics. *Biochimica Biophysica Acta - Mol. Cell Res.* 1866 (7), 1068–1078. doi:10.1016/j.bbamcr.2018.10.016
- Samal, A. B., Adzerikho, I. D., Mroček, A. G., and Loiko, E. N. (2000). Platelet aggregation and change in intracellular Ca (2+) induced by low frequency ultrasound *in vitro*. *Eur. J. Ultrasound* 11 (1), 53–59. doi:10.1016/s0929-8266(99)00077-4

- Soerjomataram, I., and Bray, F. (2021). Planning for tomorrow: Global cancer incidence and the role of prevention 2020-2070. *Nat. Rev. Clin. Oncol.* 18 (10), 663–672. doi:10.1038/s41571-021-00514-z
- Sun, S., Sun, S., Sun, Y., Wang, P., Zhang, J., Du, W., et al. (2019). Bubble-manipulated local drug release from a smart thermosensitive cerasome for dual-mode imaging guided tumor chemo-photothermal therapy. *Theranostics* 9 (26), 8138–8154. doi:10.7150/thno.36762
- Sun, W., Yu, H., Wang, D., Li, Y., Tian, B., Zhu, S., et al. (2021). MnO<sub>2</sub> nanoflowers as a multifunctional nano-platform for enhanced photothermal/photodynamic therapy and MR imaging. *Biomater. Sci.* 9 (10), 3662–3674. doi:10.1039/d1bm00033k
- Wang, M., Zhou, B., Wang, L., Zhou, F., Smith, N., Saunders, D., et al. (2020). Biodegradable pH-responsive amorphous calcium carbonate nanoparticles as immunoadjuvants for multimodal imaging and enhanced photoimmunotherapy. *J. Mat. Chem. B* 8 (36), 8261–8270. doi:10.1039/d0tb01453b
- Wang, Y., Bi, K., Shu, J., Liu, X., Xu, J., and Deng, G. (2019). Ultrasound-controlled DOX-SiO<sub>2</sub> nanocomposites enhance the antitumor efficacy and attenuate the toxicity of doxorubicin. *Nanoscale* 11 (10), 4210–4218. doi:10.1039/c8nr08497a
- Wang, Z., Duan, Y., and Duan, Y. (2018). Application of polydopamine in tumor targeted drug delivery system and its drug release behavior. *J. Control. Release* 290, 56–74. doi:10.1016/j.jconrel.2018.10.009
- Wen, G., Li, X., Zhang, Y., Han, X., Xu, X., Liu, C., et al. (2020). Effective phototheranostics of brain tumor assisted by near-infrared-II light-responsive semiconducting polymer nanoparticles. *ACS Appl. Mat. Interfaces* 12 (30), 33492–33499. doi:10.1021/acsami.0c08562
- Wen, M., Ouyang, J., Wei, C., Li, H., Chen, W., and Liu, Y. N. (2019). Artificial enzyme catalyzed cascade reactions: Antitumor immunotherapy reinforced by NIR-II light. *Angew. Chem. Int. Ed.* 58 (48), 17425–17432. doi:10.1002/anie.201909729
- Weyergang, A., Cheung, L. H., Rosenblum, M. G., Mohamedali, K. A., Peng, Q., Waltenberger, J., et al. (2014). Photochemical internalization augments tumor vascular cytotoxicity and specificity of VEGF (121)/rGel fusion toxin. *J. Control. Release* 180, 1–9. doi:10.1016/j.jconrel.2014.02.003
- Yang, G., Xu, L., Chao, Y., Xu, J., Sun, X., Wu, Y., et al. (2017). Hollow MnO<sub>2</sub> as a tumor-microenvironment-responsive biodegradable nano-platform for combination therapy favoring antitumor immune responses. *Nat. Commun.* 8 (1), 902. doi:10.1038/s41467-017-01050-0
- Yasothamani, V., Karthikeyan, L., Shyamsivappan, S., Haldorai, Y., Seetha, D., and Vivek, R. (2021). Synergistic effect of photothermally targeted NIR-responsive nanomedicine-induced immunogenic cell death for effective triple negative breast cancer therapy. *Biomacromolecules* 22 (6), 2472–2490. doi:10.1021/acs.biomac.1c00244
- Yu, L., Hu, P., and Chen, Y. (2018). Gas-generating nanoplatfoms: Material Chemistry, multifunctionality, and gas therapy. *Adv. Mat.* 30 (49), e1801964. doi:10.1002/adma.201801964
- Zhang, F., Li, F., Lu, G. H., Nie, W., Zhang, L., Lv, Y., et al. (2019). Engineering magnetosomes for ferroptosis/immunomodulation synergism in cancer. *ACS Nano* 13 (5), 5662–5673. doi:10.1021/acs.nano.9b00892
- Zhang, W. X., Hao, Y. N., Gao, Y. R., Shu, Y., and Wang, J. H. (2021). Mutual benefit between Cu (II) and polydopamine for improving photothermal-chemodynamic therapy. *ACS Appl. Mat. Interfaces* 13 (32), 38127–38137. doi:10.1021/acsami.1c12199
- Zhao, H., Zhang, G., Chong, S., Zhang, N., and Liu, Y. (2015). MnO<sub>2</sub>/CeO<sub>2</sub> for catalytic ultrasonic decolorization of methyl orange: Process parameters and mechanisms. *Ultrason. Sonochem.* 27, 474–479. doi:10.1016/j.ultsonch.2015.06.009
- Zheng, P., Ding, B., Jiang, Z., Xu, W., Li, G., Ding, J., et al. (2021). Ultrasound-augmented mitochondrial calcium ion overload by calcium nanomodulator to induce immunogenic cell death. *Nano Lett.* 21 (5), 2088–2093. doi:10.1021/acs.nanolett.0c04778
- Zhou, T., Liang, X., Wang, P., Hu, Y., Qi, Y., Jin, Y., et al. (2020). A hepatocellular carcinoma targeting nanostrategy with hypoxia-ameliorating and photothermal abilities that, combined with immunotherapy, inhibits metastasis and recurrence. *ACS Nano* 14 (10), 12679–12696. doi:10.1021/acs.nano.0c01453